WILEY VCH

RESEARCH ARTICLE

Nickel-Mediated Synthesis of Fused Heterocycle-Linked Covalent Organic Frameworks for Self-sensitized Photocatalysis

Xiaofei Zhang,[a#] Yu Tang,[b#] Caoyu Yang,[c] Zhenghao Li,[b] Danjun Fu,[b] Lulu Wang, Le Yang,[a*] Jishan Wu,[b*] Zhu Jun[a*]

[#]These authors contributed equally to this work.

[a] Dr. X. Zhang, Prof. Dr. L. Yang and Dr. J. Zhu
Institute of Materials Research and Engineering (IMRE) Agency for Science, Technology and Research (A*STAR) 2 Fusionopolis Way, Singapore 138634
E-mail: zhuj@imre.a-star.edu.sg; yangle@imre.a-star.edu.sg

[b] Y. Tang, Z. Li, D. Fu, L. W and Prof. Dr. J. Wu
Department of Chemistry, National University of Singapore 3 Science drive 3, Singapore 117543
E-mail: chmwuj@nus.edu.sg

[c] Dr. C. Y
Laboratory of Nanosystem and Hierarchical Fabrication, National Center for Nanoscience and Technology Beijing 100190, P. R. China

Supporting information for this article is given via a link at the end of the document.

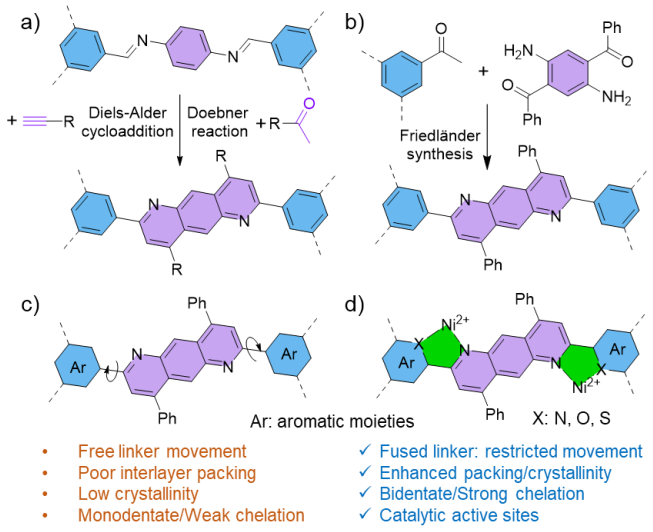
Abstract: Conjugated and chemically robust covalent organic frameworks (COFs) incorporating metal ions hold great promise in diverse applications due to their finely tuned optoelectronic properties. However, their synthesis typically relies on post-synthetic modifications to stabilize linkages and introduce chelation sites, and metal incorporation is almost exclusively achieved through post-synthetic chelation of pre-formed COFs. Such approaches often result in compromised crystallinity, incomplete conversion and limited control over modification sites. Here, we report a direct, one-pot nickel-mediated Friedländer annulation strategy to construct Ni-chelated fused heterocycle-linked COFs (**NNiN**, **NNiO** and **NNiS**). The fused heterocycle linkages act as an additional structural regulation factor, enabling precise tuning of framework packing and metal-chelation environment, thereby enhancing crystallinity and optoelectronic properties simultaneously. The resulting COFs exhibit extended π-conjugation, efficient Ni chelation and strong charge-transfer absorption in the visible-light region. Combining conjugated robust linkages, accessible single-site Ni centers, and self-photosensitizing capability, these frameworks provide a powerful platform for photocatalysis. They achieved up to 98% conversion in carbon-chalcogen coupling reactions, while retaining crystallinity and catalytic activity over multiple cycles. This work thus offers a general strategy for designing stable, π-conjugated and metal-functionalized COFs, broadening opportunities for heterogeneous catalysis and beyond.

Introduction

Covalent organic frameworks (COFs) are crystalline porous materials constructed from covalently linked organic building blocks, featuring high surface area, tunable functionality, and designable pore architectures that enable broad applications including optoelectronics,[1] gas adsorption/separation,[2, 3] energy storage,[4] biomedicine,[5] sensing[6] and catalysis.[7] Early COFs were mainly built from reversible covalent bonds (e.g., imines and boronate esters), leading to the extensive use of aldehyde, amino, boronate ester, and boroxine monomers to achieve diverse structures and functions.[8-10] To further enrich COF architectures, less reversible linkages such as olefin,[11-13] aminal/amine,[14,15] C-C,[16] triazine,[17] pyrazine,[18,19] β-ketoenamine,[20] imidazole,[21] diyne,[22] and dioxin[23] have since been developed.

The crystallinity of COFs typically relies on dynamic covalent chemistry, but the inherent instability of these bonds often causes structural collapse in aqueous, acidic, or basic media and in the presence of guest molecules,[24] thereby limiting their use under practical conditions. Imine-linked (C=N) COFs are generally more stable than boron-based analogues, yet their stability remains insufficient for practical applications. To overcome this limitation, strategies have been developed to convert labile C=N bonds into more robust linkages; for example, post-synthetic modifications can transform imines into quinoline,[25,26] amide,[27] benzoxazole,[28] or benzothiazole[29] units. These approaches typically involve first constructing an ordered imine framework, followed by secondary reactions such as cyclization or oxidation, but they often require harsh conditions that risk structural defects, incomplete conversion, and low efficiency.

To address these issues, self-locking strategies have been employed to construct fused heterocycle-linked COFs, where intramolecular cyclization reactions (e.g., Wang's cascade sequence of Schiff-base condensation, [4+2] cycloaddition, and dehydroaromatization,[30] and Banerjee's one-pot imine condensation/nucleophilic substitution/Friedel-Crafts protocol[31]) yield frameworks with enhanced structural packing and robustness. In parallel, multicomponent reactions provide an efficient strategy for constructing practically useful COFs, as they combine atom economy, rapid reaction kinetics, and simplified synthesis while enabling the formation of diverse heterocyclic linkages. The incorporation of heterocycles not only facilitates the generation of structurally robust frameworks but also enhances crystallinity through improved structural packing, which is promoted by more pronounced weak intermolecular interactions.



Scheme 1. a) The reported strategies to convert imine linkages to quinoline linkages by post-modification reactions of pre-formed COFs; b) Our previously reported one-pot strategy to prepare quinoline-linked macrocycles and COFs; c) Illustration of free linker movement resulting in poor interlayer packing; d) Nickel-mediated linkage anchoring through in situ chelation during framework formation.

Quinoline-linked COFs represent an important class of conjugated heterocyclic frameworks that endow COFs with both chemical robustness and enhanced optoelectronic properties.[25,26 32-36] While many of these materials have been synthesized by post-synthetic modifications such as Diels-Alder or Doebner cycloaddition reactions (Scheme 1a), one-pot strategies using specially functionalized monomers capable of undergoing simultaneous condensation and cyclization have also been explored. In our previous attempt, we found that the classical Friedländer synthesis, which forms quinoline derivatives through the condensation of *o*-aminoaryl carbonyl compounds with active methylene-containing carbonyl species, can yield conjugated macrocycles and two-dimensional polymers in high yield but with low crystallinity (Scheme 1b).[37] We attribute the poor crystallinity of these polymers to the irreversible nature of the Friedländer annulation, which restricts structural error correction, as well as to the high conformational freedom of the linkers (Scheme 1c), which diminishes interlayer interactions and hinder structural regulation. To overcome these limitations, we hypothesized that introducing metal ions into predesigned chelating sites within the ligands during framework construction (Scheme 1d) could enhance crystallinity. In particular, in situ coordination with nickel ions can generate rigid five-membered metallacyclic units that simultaneously restrict linker motion and strengthen interlayer interactions, thereby promoting structural regulation and directing the assembly of building blocks into more ordered crystalline architectures. In addition, the incorporation of single-site Ni^{2+} centers provides significant opportunities for catalysis,[38-40] as the π-conjugated framework backbone together with the fused metallacyclic units can modulate electron and energy transfer processes.

Herein, we report a direct, one-pot nickel-mediated Friedländer annulation strategy to construct three fused heterocycle-linked COFs (**NNiN**, **NNiO** and **NNiS**), which exhibited improved crystallinity compared with their nickel-free counterparts. These COFs, with stable π-conjugated frameworks, accessible single-site Ni centers, self-photosensitizing and strong charge-transfer absorption in the green-light region, offer a safer and more economical platform for photocatalytic carbon-chalcogen cross-coupling reaction. Carbon-chalcogen cross-coupling reactions are industrially important for synthesizing aryl chalcogenides, key motifs in pharmaceuticals, agrochemicals, dyes, and organic electronics.[41-43] Current catalysts face challenges such as high cost (Pd-based), harsh conditions (Cu-based), need for specialized ligands, catalyst deactivation with heavier chalcogens, and limited recyclability. While Ni-based photocatalysts have been developed to achieve mild reaction conditions, they typically require external photosensitizers (Ir or Ru complexes) and UV/deep blue light, increasing cost and safety concerns, and complicating catalyst recovery.[44-46] COFs, with their porosity, tunability, stability, and recyclability, offer a promising platform, and our nickel-chelated fused-heterocycle-linked COFs could serve as effective catalysts for carbon-chalcogen cross-coupling reactions. The investigation of the photocatalytic performance of these COFs under 532 nm light irradiation in acetonitrile at room temperature demonstrated exceptional catalytic performance, achieving up to 98% conversion yield in C-S cross coupling and excellent recyclability. This work introduces a new strategy for the multi-component, one-pot construction of conjugated COFs featuring fused-heterocycle metal-chelated linkages. The generality and mildness of this approach not only expands the design of irreversible-bond COFs through additional structural regulation but also inspires the development of metal-functionalized COFs for heterogeneous catalysis and other applications.

Results and Discussion

Monomer **M1** (Figure 1a) was prepared following a reported procedure,[47] while **M2**, **M3**, and **M4** were synthesized via three-fold Suzuki coupling between 1,3,5-phenyltriboronic acid tris(pinacol) ester and the corresponding heterocyclic acetophenone halides (synthetic details and characterization data are provided in the Supporting Information). Our initial attempt employed **M1** and **M2** for COF synthesis in the absence of $NiCl_2$. A Pyrex tube charged with **M1**, **M2**, diphenyl phosphate (acid catalyst), and mesitylene/dioxane (2:1 v/v) was sonicated for 15 min, degassed by three freeze-pump-thaw cycles, sealed under vacuum, and heated at 140 °C for 5 days. After cooling to room temperature, the crude product was thoroughly washed with DCM, water, and THF for three times and dried overnight, yielding COF **NN** without Ni chelation. Taking advantage of the high tolerance and selectivity of the Friedländer annulation toward additives,[48-50] we next introduced $NiCl_2$ in situ under identical conditions, affording COF **NNiN**. Powder X-ray diffraction (PXRD) comparison of **NN** and **NNiN** (Figure S1) revealed that **NN** exhibited broad, diffuse peaks similar to the defect-prone structures reported previously, while **NNiN** displayed significantly

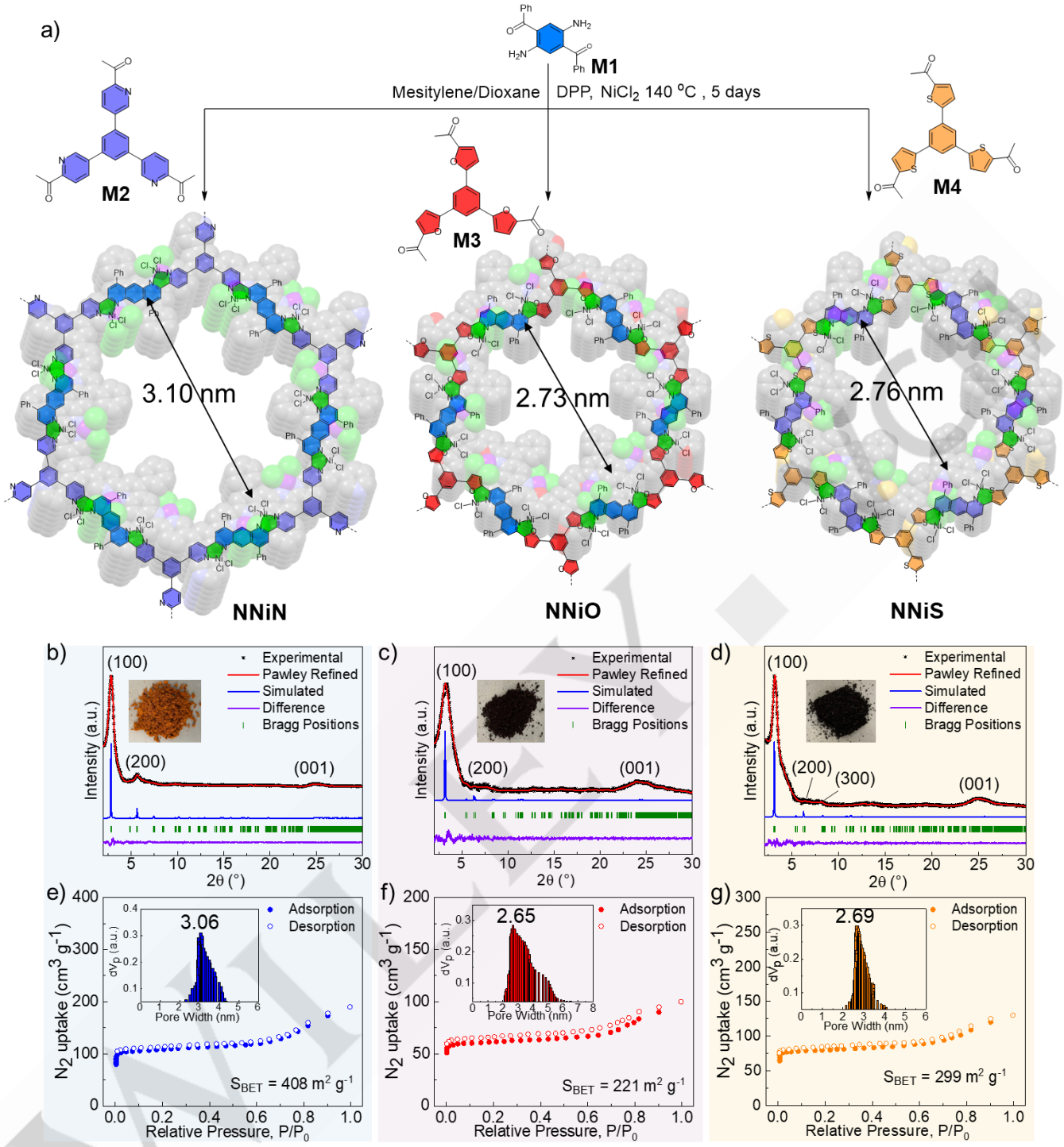


Figure 1. a) Synthetic route of COFs **NNiN**, **NNiO and NNiS**; b) c) d) PXRD data of **NNiN**, **NNiO and NNiS**: experimental (black), Pawley-refined (red), simulated (blue), difference (purple), Bragg position (green); inset is an image of the materials. e) f) g) Nitrogen sorption isotherm curves of **NNiN**, **NNiO and NNiS** measured at 77 K: inset is the corresponding pore-size distribution profile.

sharper reflections, indicating improved crystallinity. This enhancement could be attributed to the additional structural regulation imposed by Ni chelation during framework formation. Encouraged by these results, we extended this strategy to **M3** and **M4**, affording COF **NNiO** and **NNiS**, respectively, with varied heteroatomic chelation environments. This not only confirmed the generality of the Ni-mediated approach but also enabled further tuning of the COFs' optoelectronic properties. All three COFs were obtained in high yields: **NNiN** as a dark orange solid (84%), **NNiO** as a dark red solid (86%), and **NNiS** as a dark red solid (85%) (Figure 1a).

Elemental analysis was then performed to quantify the extent of Ni chelation (Table S1–S3). The measured C/N/O/S/Ni/Cl contents closely matched the theoretical values calculated from

their unit cell compositions. Ni incorporation was highly efficient, with chelation extents of 91% (**NNiN**), 86% (**NNiO**), and 88% (**NNiS**). The slightly higher Ni content in **NNiN** likely reflects the stronger chelation ability of the NN-type ligand, which decreases upon substitution with O or S donor sites. Notably, the darker color of **NNiO** and **NNiS** suggests enhanced visible-light absorption, consistent with stronger electron-donating effects of O and S and a more pronounced metal-to-ligand charge transfer process.[51-53]

The chemical structures of **NNiN**, **NNiO** and **NNiS** were confirmed by Fourier transform infrared (FTIR) spectroscopy (Figures S2–S4) and solid-state ^{13}C cross-polarization magic-angle spinning (CP-MAS) NMR spectroscopy (Figure S5). In the FTIR spectra, the characteristic -NH_2 stretching vibrations at 3464 and 3374 cm^{-1} and the C=O vibration at 1650–1690 cm^{-1} observed in the monomers disappeared in the COFs, indicating complete monomer consumption. Meanwhile, a new band at ~1592 cm^{-1} corresponding to aza-ring C=N stretching was clearly observed in all three COFs. The ^{13}C CP-MAS NMR spectra further supported these results: no resonances above 160 ppm attributable to C=O or Schiff-base C=N carbons were detected, while signals at ~150 ppm, corresponding to carbons adjacent to electron-withdrawing atoms in the heterocyclic rings, confirmed successful heterocycle formation. Thermogravimetric analysis (TGA) revealed good thermal stability, with significant weight loss occurring only above 300-400 °C (Figure S6).

The COFs crystallinity was manifested by experimental and simulated PXRD patterns (Figure 1b-1d). The reflection at 2.82°, 5.66° and 24.6° for **NNiN** can be attributed to the (100), (200) and (001) plane, respectively. Good agreement was found between the simulated PXRD pattern and experimentally measured pattern. Pawley refinement was performed, resulting in the unit cell parameters of a = 36.42 Å, b = 36.19 Å, c = 3.61 Å, α = 90.3°, β =86.2°, γ =120.8°, with agreement factors of R_{wp} = 5.56%, R_p = 3.71%. The reflection at 3.22°, 6.44° and 24.1° for **NNiO** can be attributed to the (100), (200) and (001) plane, respectively. Good agreement was found between the simulated PXRD pattern and experimentally measured pattern. Pawley refinement was performed, resulting in the unit cell parameters of a = 31.9 Å, b = 32.6 Å, c = 3.68 Å, α = 89.7°, β =86.4°, γ =120.5°, with agreement factors of R_{wp} = 5.54%, R_p = 4.12%. The reflection at 3.21°, 6.42° 8.49° and 24.1° for **NNiS** can be attributed to the (100), (200), (210) and (001) plane, respectively. Good agreement was found between the simulated PXRD pattern and experimentally measured pattern. Pawley refinement was performed, resulting in the unit cell parameters of a = 32.6 Å, b = 32.9 Å, c = 3.68 Å, α = 95.5°, β =84.2°, γ =122.3°, with agreement factors of R_{wp} = 5.69%, R_p = 3.84%. The Brunauer-Emmett-Teller (BET) surface areas derived from their nitrogen sorption isotherm at 77 K were determined to be 408, 221 and 299 m^2/g, respectively for **NNiN**, **NNiO** and **NNiS** (Figure 1e-1g). The isotherm displayed a rise in the low-pressure range, generating a typical type-I nitrogen sorption isotherm. The relatively modest BET surface areas of these COFs can be attributed to two main factors: the irreversible nature of Friedländer annulation, which may form amorphous domains, and the formation of macrocycles of varying sizes (predominantly hexagons, but also kinetically stable pentagons and heptagons), as revealed in our previous findings,[37] which introduces structural defects. Together, these effects reduce the accessible surface area compared to the idealized framework. Nevertheless, the pore size distributions determined by non-local density function theory (NLDFT) revealed size distribution profiles centered at 3.06, 2.65 and 2.69 nm, respectively for **NNiN**, **NNiO**,

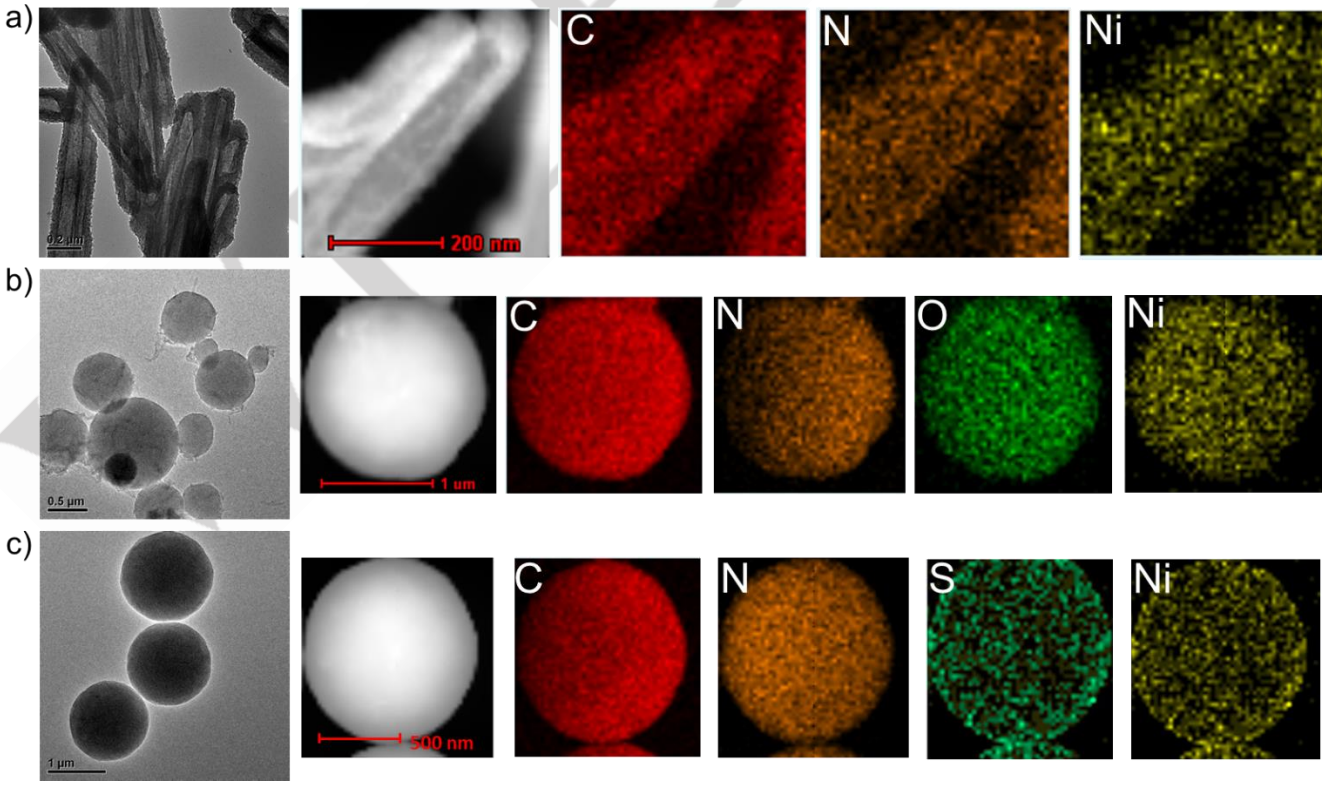


Figure 2. STEM images and STEM-EDX elemental mapping of a) **NNiN**, b) **NNiO**, and c) **NNiS**.

and **NNiS** (Figure 1e-1g, the insets), matching well with the simulated theoretical pore sizes (Figure 1a). Moreover, the pore size distribution of **NNiO** appeared broader than that of **NNiN** and **NNiS**, which can be attributed to the weaker chelation strength of O sites compared with N and S sites. This is consistent with the slightly more broadened PXRD pattern observed for **NNiO**. The weaker chelation likely renders the nickel-chelated fused heterocyclic linkages less rigid, thereby reducing structural regulation during framework formation and affecting both crystallinity and pore size distribution.

The scanning electron microscopy (SEM) images revealed distinct morphologies: **NNiN** exhibited a fiber-like structure, whereas **NNiO** and **NNiS** showed spherical morphologies (Figure S7). This difference could be attributed to the polarity of the framework skeletons. The higher polarity of **NNiN** skeleton, arising from the greater content of pyridine units, likely promotes anisotropic growth into fibers. In contrast, the incorporation of less polar furan and thiophene units in **NNiO** and **NNiS** reduces overall polarity, favoring the formation of more isotropic, spherical particles. The scanning transmission electron microscopy (STEM) images demonstrated similar morphologies of these COFs (Figure 2a-2c). To evaluate the dispersion of the single-site Ni atoms in the COF materials, energy-dispersive X-ray (EDX) elemental mapping analysis was performed, which showed uniform distribution of respective C/N/O/S/Ni across the samples (Figure 2a-2c).

X-ray absorption spectroscopy (XAS) was utilized to elucidate the electronic structures and local chemical environment of the Ni atoms (Figure 3a). The Ni K-edge X-ray absorption near-edge structure (XANES) spectra of **NNiN**, **NNiO** and **NNiS** were measured, with Ni foil and $NiCl_2$ hexahydrate as references. The absorption edge position of Ni in **NNiN**, **NNiO** and **NNiS** closely matched with $NiCl_2$ rather than Ni foil, indicating that the Ni in the prepared COF materials was in a valence of +2 (Figure 3b). More detailed structural information was obtained from the Fourier transform extended X-ray absorption fine structure (FT-EXAFS) spectra (Figure 3c). The *R*-space spectra of Ni in COFs exhibited a distinct peak at about 1.6 Å, in accordance with the first coordination shell of Ni-heteroatom. Meanwhile, the absence of the peak at about 2.2 Å for Ni-Ni indicated that the Ni sites in COFs were well atomically dispersed. Quantitative EXAFS analysis was conducted to analyze structural parameters (Figure 3d-3f, S10-S12, Table S4-S6). The results illustrated that: one Ni atom is chelated with two N atoms with an atomic distance of 1.967 Å for **NNiN**; one Ni atom is chelated with one N atom and one O atom with an atomic distance of 1.953 and 1.985 Å, respectively, for **NNiO**; one Ni atom is chelated with one N atom and one S atom with an atomic distance of 1.922 and 2.266 Å, respectively, for **NNiS**. Besides, each Ni atom in all three COFs was bonded with two Cl counter ions with an atomic distance around 2.382 Å and found to complex with two water molecules with an atomic distance around 2.071 Å. These results confirmed the Ni-chelated configuration in the COFs, evidencing the formation of designed Ni-chelated fused heterocyclic linkages.

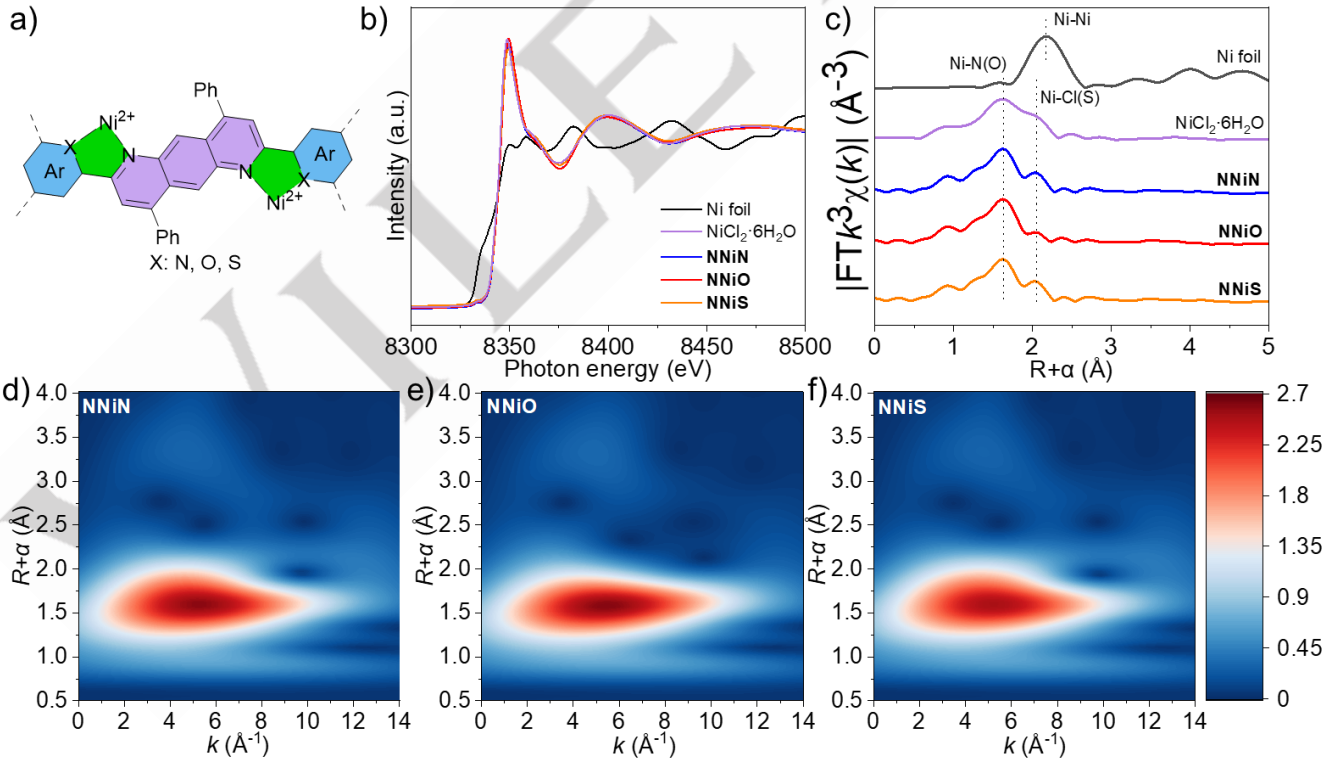


Figure 3. a) Structure of the nickel-chelated fused heterocyclic linkages; b) XANES spectra of **NNiN**, **NNiO**, and **NNiS**, with Ni foil and $NiCl_2$ hexahydrate as references; c) k3 weighted Ni K-edge FT-EXAFS spectra of **NNiN**, **NNiO**, and **NNiS**, with Ni foil and $NiCl_2$ hexahydrate as references; d) e) f) k3 weighted EXAFS wavelet transform contour plots for **NNiN**, **NNiO**, and **NNiS**.

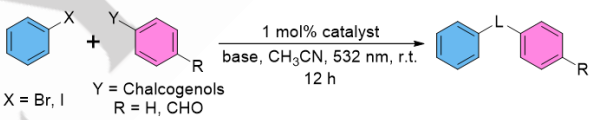
The solid-state diffuse reflectance UV-vis spectra of these COFs showed strong absorption across the visible-light region, with maxima around 500-550 nm (Figure S13a). Compared with **NNiN**, both **NNiO** and **NNiS** exhibited red-shifted absorption, which can be ascribed to the stronger electron-donating character of O and S sites that enhance the metal-to-ligand charge transfer process. The optical energy gaps, estimated from Kubelka–Munk (K–M) plots, were 1.51, 1.91, and 1.75 eV for **NNiN**, **NNiO** and **NNiS**, respectively. The relatively smaller gap of **NNiN** is likely due to its more planar N-Ni-N chelation geometry, which preserves conjugation across the fused heterocyclic linkages. Cyclic voltammetry (CV) measurements of **NNiN**, **NNiO** and **NNiS** were carried out in acetonitrile with 0.1 M Bu_4NPF_6 as the supporting electrolyte, using Ag/AgCl as the reference electrode, glassy carbon as the working electrode, and a Pt wire as the counter electrode, at a scan rate of 10 mV s^{-1}. Ferrocene (Fc) was used as an internal reference for determining HOMO and LUMO energy levels. All three COFs displayed irreversible redox behavior, with reduction onsets at -0.86, -1.02, and -1.14 V vs. Fc/Fc^+ for **NNiN**, **NNiO**, and **NNiS**, respectively (Figure S14). For comparison, the reduction of Ni^{2+} ions typically occur between -1.2 to -1.9 V depending on the coordination environment.[39,54] The earlier reduction potentials observed here suggests that the reductions are primarily associated with the electron-deficient framework skeletons rather than the Ni^{2+} centers. This assignment is consistent with theoretical calculations showing that the LUMO levels are localized mainly on the framework skeletons (Figure S15-S17). Nevertheless, the broad reduction feature spanning around -1.2 to -1.8 V likely arises from overlapping contributions of both the framework skeletons and the Ni^{2+} sites. By combining the UV-vis and CV results, the LUMO/HOMO energy levels were estimated to be -3.94/-5.54 eV for **NNiN**, -3.78/-5.69 eV for **NNiO**, and -3.66/-5.41 eV for **NNiS**.

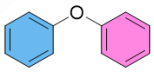
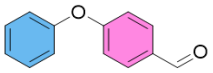
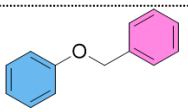
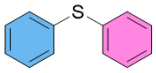
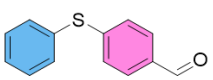
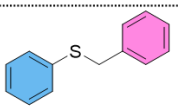
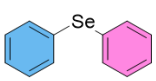
Carbon-chalcogen cross-coupling is industrially valuable but existing catalysts often suffer from high cost, harsh conditions, and poor recyclability, while Ni-based photocatalysts still rely on expensive photosensitizers and UV/blue light. These COFs, with stable conjugated frameworks, accessible single-site Ni centers, self-photosensitizing and strong charge-transfer absorption in the green-light region, offer a safer and more economical platform for photocatalytic carbon-chalcogen cross-coupling reaction. The cross-coupling reactions between aryl halides (Br or I) and various chalcogenols (-OH, -SH, -SeH) were evaluated in acetonitrile at room temperature using 1 mol% COF catalyst and a suitable base under 532 nm LED irradiation (30 W, overnight). The choice of base is critical, as it governs nucleophile deprotonation, stabilization of catalytic intermediates, and ultimately reaction selectivity and yield.[55,56] To identify the optimal base, we examined the coupling of bromobenzene with phenol using **NNiN** as the catalyst (Table S7). Overall, organic bases outperformed inorganic ones, with diisopropylamine ($^iPr_2NH$) affording the highest conversion. This can be attributed to its moderate basicity, sufficient steric hindrance to suppress side reactions, and weak coordination that avoids Ni site poisoning. For comparison, $NiCl_2$ was tested under identical conditions and gave <5% conversion. Furthermore, control experiments showed that performing the reaction with **NNiN** in the dark resulted in only trace conversion, confirming that the transformation proceeds photocatalytically under the designed conditions.

We then expanded the substrate scope, as summarized in Table 1, using various aryl halides, chalcogenols, and the three COF catalysts with different Ni-chelation environments. Overall, the COF catalysts showed promising conversion yields under the designed conditions, with **NNiS** achieving up to 98% yield. While aryl iodides sometimes gave slightly higher conversions than aryl bromides, the difference was generally minor, indicating that these COF catalysts can efficiently activate aryl halides regardless of their different intrinsic reactivity. Both C-S and C-Se couplings proceeded more efficiently than C-O couplings, and **NNiS** and **NNiN** consistently outperformed **NNiO**. These trends across substrates and catalysts provide valuable insights for optimizing reaction conditions and probing mechanistic pathways.

Formation of radical species is central to many photocatalytic systems;[57-59] thus, 2,2,6,6-Tetramethylpiperidine 1-oxyl (TEMPO), a common radical scavenger, was added to selected reactions (entries 1, 4, and 7 in Table 1). In all cases, only trace conversion was observed, indicating the involvement of radical intermediates. To gain further insights, in situ electron paramagnetic resonance (EPR) spectroscopy was employed. Considering the superior performance of **NNiS** in C-S coupling and the generally longer lifetimes of sulfur-centered radicals, the coupling of bromobenzene with thiophenol using **NNiS** (entry 4, Table 1) was chosen for detailed monitoring. First, the **NNiS** catalyst suspended in acetonitrile without substrates was examined under dark and irradiated conditions, with spectra collected every 3 min

Table 1. Various carbon-chalcogen cross-coupling reactions using **NNiN**, **NNiO** and **NNiS** COF catalysts under green light (532 nm) irradiation.



Product	Entry	Catalyst	Yield (%) X=Br	Yield (%) X=I
	1	NNiN	83	85
		NNiO	72	69
		NNiS	77	80
	2	NNiN	73	74
		NNiO	59	55
		NNiS	66	63
	3	NNiN	79	78
		NNiO	68	70
		NNiS	75	77
	4	NNiN	94	95
		NNiO	82	83
		NNiS	98	98
	5	NNiN	90	91
		NNiO	81	84
		NNiS	98	97
	6	NNiN	84	87
		NNiO	72	77
		NNiS	91	93
	7	NNiN	89	90
		NNiO	71	74
		NNiS	94	95

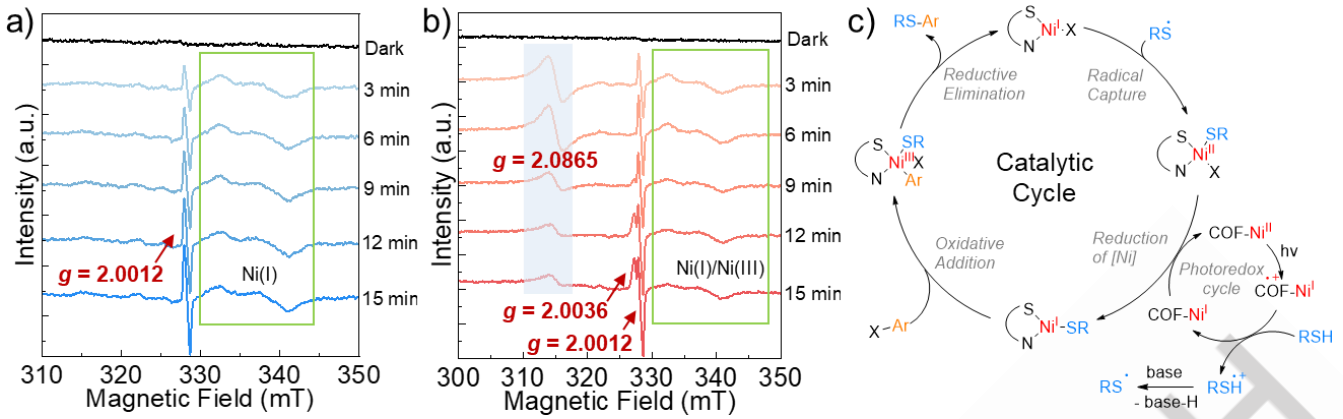


Figure 4. a) b) The in situ EPR monitoring of the reaction intermediates for mechanistic investigation using the reaction between bromobenzene and thiophenol. c) The proposed reaction catalytic cycle using the COF catalysts.

(Figure 4a). No resonance was observed in the dark, whereas upon irradiation a sharp peak at 328 mT (g = 2.0012), corresponding to carbon radicals, appeared and intensified with time. Concurrently, a weak resonance at 332-343 mT was detected, attributable to Ni(I) species.[60] Since Ni(II) is EPR silent due to its diamagnetism, this observation suggests that light excitation of **NNiS** promotes electron transfer from the COF backbone to Ni(II), generating Ni(I) sites for substrate activation while leaving behind COF radical cations and suggesting the role of **NNiS** as photosensitizer. Subsequently, the reaction mixture consisting of bromobenzene and thiophenol was investigated under identical conditions (Figure 4b). Again, no signal was detected in the dark, but after 3 min irradiation a new peak at 315 mT (g = 2.0865) appeared, characteristic of thiyl radicals, alongside the carbon-centered radical signal at 328 mT (g = 2.0012). Upon prolonged irradiation (3-15 min), the thiyl radical signal gradually decreased and plateaued after ~12 min, while a new shoulder peak at g = 2.0036 emerged near the carbon-centered radical region, increasing in intensity as the thiyl radical diminished. This trend suggests that thiyl radicals are rapidly consumed, likely through coordination to Ni active sites, leading to a redistribution of carbon radical cations in distinct environments, thereby giving rise to the new carbon radical signal. The weak resonance observed at 332–343 mT could arise from both Ni(I) and Ni(III) species, which are difficult to distinguish due to their transient nature as reaction intermediates.

According to these findings and with reference to reported Ni-based cross-coupling mechanisms,[46] a plausible catalytic cycle can be proposed (Figure 4c). Upon photon absorption, the COF-Ni(II) catalyst becomes excited and transfers an electron from COF skeleton to the Ni(II) site, generating COF$^{\cdot+}$-Ni(I). The resulting carbon radical cation subsequently oxidizes R-SH, forming an RS$^{\cdot}$ radical with the assistance of a base, while regenerating COF-Ni(I), which is then ready to coordinate with substrates and enter the main catalytic cycle. In this cycle, Ni(I) captures the RS$^{\cdot}$ radical and form Ni(II)–SR/X. Reduction via the photoredox pathway affords Ni(I)-SR, which undergoes oxidative addition with the aryl halide to yield a Ni(III)-SR/Ar/X intermediate. This intermediate then undergoes reductive elimination to produce the desired coupling product while regenerating the active catalytic species. This proposed mechanism rationalizes the observed catalytic variations. The higher efficiency of C-S and C-Se coupling compared to C-O coupling can be attributed to the greater stability and easier generation of S and Se radicals. Likewise, the superior performance of **NNiS** can be explained by the additional stabilization of radicals and related intermediates imparted by the S-chelation sites.

The recyclability of these catalysts was evaluated using the reaction conditions of entry 4 in Table 1 (Figure S18). The results revealed excellent reusability, with only a slight decrease in catalytic conversion yield after successive cycles. In addition, the PXRD patterns recorded before and after catalysis showed a high degree of structural retention (Figure S19-S21), confirming the robustness and stability of the COF frameworks under the reaction conditions.

Conclusion

In summary, we developed a one-pot nickel-mediated Friedländer annulation strategy to construct Ni-chelated fused-heterocycle-linked COFs (**NNiN**, **NNiO** and **NNiS**), in which the linkages serve as an additional structural regulation factor, enabling precise tuning of the metal-ligand environment and structural packing for enhanced crystallinity and optoelectronic properties. These COFs exhibited excellent photocatalytic performance, achieving high conversion yields and robust recyclability in carbon-chalcogen cross-coupling reactions, demonstrating their potential as cost-effective and sustainable heterogeneous photocatalysts. Furthermore, this general and mild synthetic approach expands the design space of irreversible COFs and provides a versatile platform for creating advanced metal-functionalized frameworks for catalysis and other applications.

Acknowledgements

This work was financially supported by A*STAR Career Development Fund (C233312013) and MTC A*STAR Young Individual Research Grant (M23M7c0118) (to J.Z.); MOE Tier 3 program (MOE-000755-00) (to J.W.); National Research Foundation Fellowship (NRF-NRFF15-2023-0011) and MTC Programmatic Fund (M24M9b0013) (to L.Y.)

Keywords: Conjugated COFs • Fused-heterocycle linkages • Metalation of COFs • Carbon-chalcogen cross-coupling

[1] N. Keller, T. Bein, *Chem. Soc. Rev.* **2021**,*50,* 1813.

[2] Z. Zhou, T. Ma, H. Zhang, S. Chheda, H. Li, K. Wang, S. Ehrling, R. Giovine, C. Li, A. H. Alawadhi, M. M. Abduljawad, M. O. Alawad, L. Gagliardi, J. Sauer, O. M. Yaghi, *Nature* **2024**, *635*, 96-101.

[3] Y. Zhang, H. Wang, W. Wang, Z. Zhou, J. Huang, F. Yang, Y. Bai, P. Sun, J. Ma, L. E. Peng, C. Y. Tang, L. Shao, *Matter* **2024**, *7*, 1406-1439.

[4] M. Wang, G. Wang, C. Naisa, Y. Fu, S. M. Gali, S. Paasch, M. Wang, H. Wittkaemper, C. Papp, E. Brunner, S. Zhou, D. Beljonne, H. P. Steinruck, R. Dong, X. Feng, *Angew. Chem. Int. Ed.* **2023**, *62*, e202310937.

[5] L. L. Zhou, Q. Guan, Y. B. Dong, *Angew. Chem. Int. Ed.* **2023**, *63*, e202314763.

[6] T. Skorjanc, D. Shetty, M. Valant, *ACS Sensors* **2021**, *6*, 1461-1481.

[7] R. Liu, D. Zhao, S. Ji, H. Shao, Y. Chen, M. Feng, T. Wang, J. Li, M. Lin, T. C. Sum, N. Yan, S. Seki, D. Jiang, *Nat. Mater.* **2025**, *24*, 1245-1257.

[8] A. P. Cote, A. I. Benin, N. W. Ockwig, M. O'Keeffe, A. J. Matzger, O. M. Yaghi, *Science* **2005**, *310*, 1166-1170.

[9] H. M. E-. Kaderi, J. R. Hunt, J. L. M-. Cortes, A. P. Cote, R. E. Taylor, M. O'Keeffe, O. M. Yaghi, *Science* **2007**, 31*6*, 268-272.

[10] S. Y. Ding, J. Gao, Q. Wang, Y. Zhang, W. G. Song, C. Y. Su, W. Wang, *J. Am. Chem. Soc.* **2011**, *133*, 19816-19822.

[11] E. Jin, M. Asada, Q. Xu, S. Dalapati, M. A. Addicoat, M. A. Brady, H. Xu, T. Nakamura, T. Heine, Q. Chen, D. Jiang, *Science*, **2017**, *357*, 673-676.

[12] X. Zhuang, W. Zhao, F. Zhang, Y. Cao, F. Liu, S. Bi, X. Feng, *Polym. Chem.* **2016**, **7**, 4176-4181.

[13] S. Bi, P. Thiruvengadam, S. Wei, W. Zhang, F. Zhang, L. Gao, J. Xu, D. Wu, J. S. Chen, F. Zhang, *J. Am. Chem. Soc.* **2020**, *142*, 11893-11900.

[14] L. Grunenberg, G. Savasci, M. W. Terban, V. Duppel, I. Moudrakovski, M. Etter, R. E. Dinnebier, C. Ochsenfeld, B. V. Lotsch, *J. Am. Chem. Soc.* **2021**, *143*, 3430-3438.

[15] S.-Y. Jiang, S.-X. Gan, X. Zhang, H. Li, Q.-Y. Qi, F.-Z. Cui, J. Lu, X. Zhao, *J. Am. Chem. Soc.* **2019**, *141*, 14981-14986.

[16] C. Yuan, S. Fu, K. Yang, B. Hou, Y. Liu, J. Jiang, Y. Cui, *J. Am. Chem. Soc.* **2020**, *143*, 369-381.

[17] Y. Ren, S. Yang, Y. Xu, *Acc. Chem. Res.* **2025**, *58*, 474-487.

[18] M. Wang, M. Ballabio, M. Wang, H. H. Lin, B. P. Biswal, X. Han, S. Paasch, E. Brunner, P. Liu, M. Chen, M. Bonn, T. Heine, S. Zhou, E. Canovas, R. Dong, X. Feng, *J. Am. Chem. Soc.* **2019**, *141*, 16810-16816.

[19] J. Guo, Y. Xu, S. Jin, L. Chen, T. Kaji, Y. Honsho, M. A. Addicoat, J. Kim, A. Saeki, H. Ihee, S. Seki, S. Irle, M. Hiramoto, J. Gao, D. Jiang, *Nat. Commun.* **2013**, *4*, 2736.

[20] S. Kandambeth, A. Mallick, B. Lukose, M. V. Mane, T. Heine, R. Banerjee, *J. Am. Chem. Soc.* **2012**, *134*, 19524-19527.

[21] P. L. Wang, S. Y. Ding, Z. C. Zhang, Z. P. Wang, W. Wang, *J. Am. Chem. Soc.* **2019**, *141*, 18004-18008.

[22] S. Wu, M. Li, H. Phan, D. Wang, T. S. Herng, J. Ding, Z. Lu, J. Wu, *Angew. Chem. Int. Ed.* **2018**, *57*, 8007-8011.

[23] B. Zhang, M. Wei, H. Mao, X. Pei, S. A. Alshmimri, J. A. Reimer, O. M. Yaghi, *J. Am. Chem. Soc.* **2018**, *140*, 12715-12719.

[24] X. Li, S. Cai, B. Sun, C. Yang, J. Zhang, Y. Liu, *Matter* **2020**, *3*, 1507-1540.

[25] X. Zhao, H. Pang, D. Huang, G. Liu, J. Hu, Y. Xiang, *Angew. Chem. Int. Ed.* **2022**, *61*, e202208833.

[26] X. Li, C. Zhang, S. Cai, X. Lei, V. Altoe, F. Hong, J. J. Urban, J. Ciston, E. M. Chan, Y. Liu, *Nat. Commun.* **2018**, *9*, 2998.

[27] Z.-B. Zhou, X.-H. Han, Q.-Y. Qi, S.-X. Gan, D.-L. Ma, X. Zhao, *J. Am. Chem. Soc.* **2022**, *144*, 1138-1143.

[28] J.-M. Seo, H.-J. Noh, H. Y. Jeong, J.-B. Baek, *J. Am. Chem. Soc.* **2019**, *141*, 11786-11790.

[29] M. Deng, J. Chakraborty, G. Wang, K. S. Rawat, L. Bourda, J. Sun, I. Nath, Y. Ji, P. Geiregat, V. Van Speybroeck, X. Feng, P. Van Der Voort, *J. Am. Chem. Soc.* **2025**, *147*, 10219-10230.

[30] J. Feng, Y.-J. Zhang, S.-H. Ma, C. Yang, Z.-P. Wang, S.-Y. Ding, Y. Li, W. Wang, *J. Am. Chem. Soc.* **2022**, *144*, 6594-6603.

[31] K. Koner, R. Banerjee, *Nat. Syn.* **2024**, *3*, 1266-1274.

[32] Y. Yang, L. Yu, T. Chu, H. Niu, J. Wang, Y. Cai, *Nat. Commun.* **2022**, *13*.

[33] X. Zhao, H. Pang, D. Huang, G. Liu, J. Hu, Y. Xiang, *Angew. Chem. Int. Ed.* **2022**, *61*, e202208833.

[34] J.-J. Li, J.-Y. Liu, S.-Y. Gao, X. Yang, R. Cao, *J. Am. Chem. Soc.* **2025**, *147*, 21754-21763.

[35] P. Das, J. Roeser, A. Thomas, *Angew. Chem. Int. Ed.* 2023, 62 , e202304349 .

[36] H. Jiang, W. Zhang, J. Wu, Q. Wang, G. Wang, P. O'Neill, S. R. Dubbaka, J. Wu, *Nat. Commun.* **2025**, *16*, 4716.

[37] J. Zhu, S. Wu, X. Hou, J. Wu, *Angew. Chem. Int. Ed.* **2021**, *60*, 25323-25327.

[38] Y. Fan, D. W. Kang, S. Labalme, J. Li, W. Lin, *Angew. Chem. Int. Ed.* **2023**, *62*, e202218908 .

[39] Y. Fan, D. W. Kang, S. Labalme, W. Lin, *J. Am. Chem. Soc.* **2023**, *145*, 25074-25079.

[40] X. Liang, N. Fu, S. Yao, Z. Li, Y. Li, *J. Am. Chem. Soc.* **2022**, *144*, 18155-18174.

[41] I. P. Beletskaya, V. P. Ananikov, *Chem. Rev.* **2011**, *111*, 1596-1636.

[42] I. P. Beletskaya, V. P. Ananikov, *Chem. Rev.* **2022**, *122*, 16110-16293.

[43] R. Bhanja, S. K. Bera, P. Mal, *Adv. Synth. Catal.* **2023**, *366*, 168-182.

[44] J. B. Diccianni, T. Diao, *Trends. Chem.* **2019**, *1*, 830-844.

[45] C. Zhu, H. Yue, J. Jia, M. Rueping, *Angew. Chem. Int. Ed.* **2021**, *60*, 17810-17831.

[46] M. D. Palkowitz, M. A. Emmanuel, M. S. Oderinde, *Acc. Chem. Res.* **2023**, *56*, 2851-2865.

[47] J. Zhu, Y. Han, Y. Ni, G. Li, J. Wu, *J. Am. Chem. Soc.* **2021**, *143*, 2716-2721.

[48] J. M-. Contelles, E. P-. Mayoral, A. Samadi, M. d, C, Carreiras, E. Soriano, *Chem. Rev.* **2009**, *109*, 2652–2671.

[49] C. C. Cheng, S. J. Yan, *Organic Reactions*, **1982**, 37-201.

[50] M. Godino-Ojer, A. J. López-Peinado, F. J. Maldonado-Hódar, E. Pérez-Mayoral, *ChemCatChem* **2017**, *9*, 1422-1428.

[51] A. M. Bond, R. L. Martin, A. F. Masters, *Inorg. Chem.* **1975**, *14*, 1432–1435.

[52] L. Puskar, P. E. Barran, B. J. Duncombe, G. Chapman, A. J. Stace, *J. Phys. Chem. A* **2005**, *109*, 273-282.

[53] M. Gennari, C. Duboc, *Acc. Chem. Res.* **2020**, *53*, 2753-2761.

[54] I. Zibermann, E. Maimon, H. Cohen, D. Meyerstein, *Chem. Rev.* **2005**, *105,* 2609-2625.

[55] D. -G. Y, B. -J. Li, Z. -J. Shi, *Acc. Chem. Res.* **2010**, *43*, 1486-1495.

[56] J. -P. Corbet, G. Miganni, *Chem. Rev.* **2006**, *106*, 2651-2710.

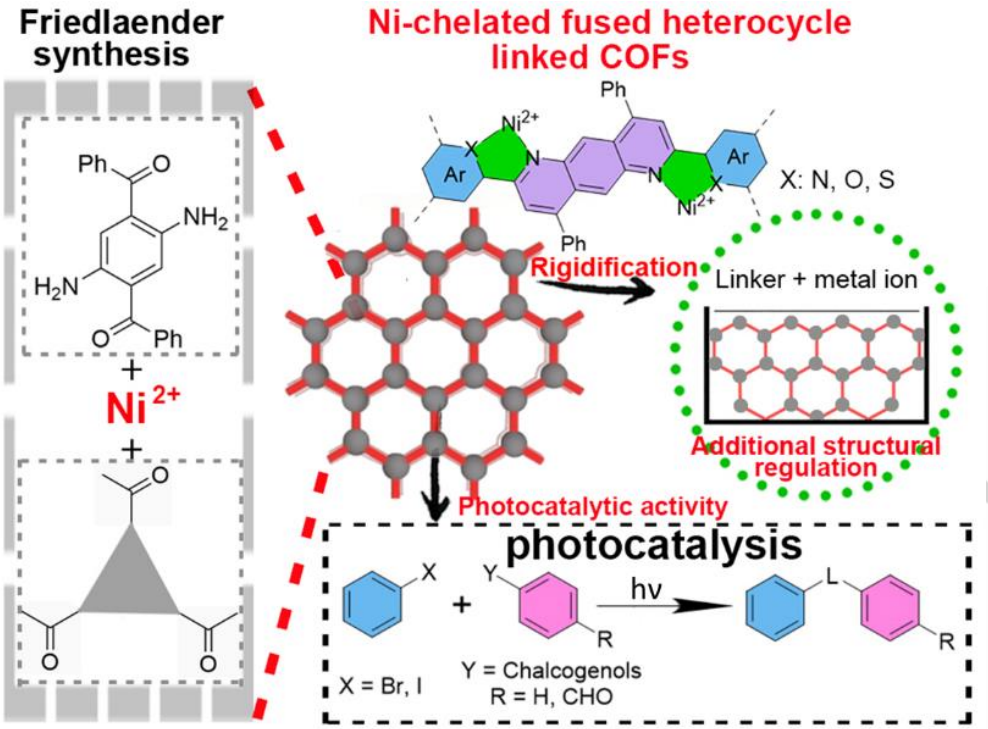
[57] H. Yi, G. Zhang, H. Wang, Z. Huang, J. Wang, A. K. Singh, A. Lei, *Chem. Rev.* **2017**, *117*, 9016-9085.

[58] Z. Wu, D. A. Pratt, *Nat. Rev. Chem.* **2023**, *7*, 573-589.

[59] W. Guo, K. Tao, W. Tan, M. Zhao, L. Zheng, X. Fan, *Org. Chem. Front.* **2019**, *6*, 2048-2066.

[60] H. Na, L. M. Mirica, *Nat. Commun.* **2022**, *13*, 1313.

Entry for the Table of Contents



We developed a direct, one-pot nickel-mediated Friedländer annulation strategy to construct Ni-chelated fused-heterocycle-linked COFs. The resulting frameworks combine structural robustness, accessible single-site Ni centers, and self-photosensitizing capability, providing a powerful platform for photocatalysis.